Supplementary Text: Linear stability analysis and evolution of immiscible fingers in homogeneous porous media

Paulo L. K. Caetano Chang[1*], Kundan Kumar[1], Arne Skauge[2], Kenneth S. Sorbie[2]

[1]Department of Mathematics, University of Bergen, Allégaten 41, Bergen, 5007, Vestland, Norway.
[2]School of Energy, Geoscience, Infrastructure and Society, Heriot-Watt University, Edinburgh, EH14 4AS, Scotland, UK.

*Corresponding author(s). E-mail(s): Paulo.Chang@student.uib.no;
Contributing authors: kundan.kumar@uib.no; a.skauge@hw.ac.uk; k.sorbie@hw.ac.uk;

S1 Linear stability analysis (LSA)

The main goal of LSA is to describe the onset (or suppression) of instability in a two-phase displacement in a porous medium. In this technique modal analysis is applied around the linearized governing equations of the flow, to determine the growth rate of small perturbations as a function of their wavenumber. The result is called the dispersion relation, and it can be used to determine the stability of the system.

The first step is to define the base-state solution, which is usually a steady-state solution of the unperturbed displacement. Then, the governing equations are linearized for small variations around the base-state solution to obtain the linearized perturbed equations. The modal analysis is then performed by decomposing the dependent variables into a base-state and small wavelike perturbations—that can grow or decay—and, after substituting these into the linearized equations, we arrive at the eigenvalue problem in terms of the disturbances.

In this section, we describe the main equations of the LSA for the incompressible, two-phase immiscible displacement in a homogeneous porous medium, as developed by Riaz and Tchelepi [1]. We consider only the case of horizontal flow (i.e. no gravity effects). The governing equations are well known and given by:

$$\phi\frac{\partial S_\alpha}{\partial t} + \nabla\cdot\boldsymbol{u}_\alpha = 0, \tag{1}$$

$$\boldsymbol{u}_\alpha = -k\frac{k_{r\alpha}}{\mu_\alpha}\nabla P_\alpha, \tag{2}$$

$$\nabla\cdot(\boldsymbol{u}_w + \boldsymbol{u}_o) = 0, \tag{3}$$

$$P_c = P_o - P_w, \tag{4}$$

where $\boldsymbol{u}_\alpha$ is the Darcy velocity of phase $\alpha(= w, o)$, ϕ is the porosity, k is the absolute permeability, $k_{r\alpha}$ is the relative permeability of phase α, μ_α is the viscosity of phase α, P_α is the pressure of phase α, and P_c is the capillary pressure.

The equations can be nondimensionalized by the following transformations:

$$\begin{aligned} \boldsymbol{x}^* &= \frac{\boldsymbol{x}}{L}, \quad \boldsymbol{u}^* = \frac{\boldsymbol{u}}{U}, \quad t^* = \frac{U}{\phi L}t, \\ \lambda_\alpha^* &= k_{r\alpha}, \quad P_\alpha^* = \frac{k}{U\mu_\alpha L}P_\alpha, \quad P_c^* = \frac{k}{U\mu_w L}P_c, \end{aligned} \tag{5}$$

where U is the injection specific discharge (or Darcy velocity).

Equations 1–4 can be rewritten as:

$$\frac{\partial S_\alpha}{\partial t^*} + \nabla_* \cdot \boldsymbol{u}_\alpha^* = 0, \tag{6}$$

$$\boldsymbol{u}_\alpha^* = \lambda_\alpha^* \nabla_* P_\alpha^*, \tag{7}$$

$$\nabla_* \cdot (\boldsymbol{u}_w^* + \boldsymbol{u}_o^*) = 0, \tag{8}$$

$$P_c^* = M P_o^* - P_w^*, \tag{9}$$

where $M = \mu_o/\mu_w$ is the viscosity ratio and $\nabla_* = \partial/\partial x_i^*$.

For convenience, we omit the asterisks from here on, with the understanding that all variables are now dimensionless.

The one-dimensional, unperturbed reference state (i.e. the base state), around which the flow equations are linearized, is derived from the moving frame formulation of the Buckley-Leverett equation, given by:

$$\frac{\partial S_w}{\partial t} + \left(\frac{\mathrm{d}F_w}{\mathrm{d}S_w} - V_s\right)\frac{\partial S_w}{\partial \xi} + \frac{\partial}{\partial \xi}\left(\frac{\lambda_w \lambda_o}{\lambda_t}\frac{\mathrm{d}P_c}{\mathrm{d}S_w}\frac{\partial S_w}{\partial \xi}\right) = 0, \tag{10}$$

where $\lambda_t = M\lambda_w + \lambda_o$ is the total mobility, $\xi = x - V_s t$ is the moving frame coordinate that moves with the shock front velocity $V_s = dF_w/dS_w(S_{ws})$, S_{ws} being the shock saturation, and F_w is the fractional flow function of the water phase,

$$F_w = \frac{M\lambda_w}{\lambda_t} = \frac{Mk_{rw}}{Mk_{rw} + k_{ro}}. \tag{11}$$

The base-state solution is the steady-state solution of Equation 10, given by:

$$D_c \frac{\mathrm{d}S_w}{\mathrm{d}\xi} = V_s(S_w - S_{w0}) + F_w(S_{w0}) - F_w(S_w), \tag{12}$$

where S_{w0} is the initial water saturation and D_c is the dispersion coefficient given by:

$$D_c = \frac{\lambda_w \lambda_o}{\lambda_t}\frac{\mathrm{d}P_c}{\mathrm{d}S_w}. \tag{13}$$

The base-state pressure is given by:

$$\lambda_o \frac{\mathrm{d}P_o}{\mathrm{d}S_w} = V_s\,(S_w - S_{w0}) + F_w(S_{w0}) - 1. \tag{14}$$

The perturbed equations in terms of the water saturation and oil pressure are:

$$\frac{\partial S_w}{\partial t} - V_s\frac{\partial S_w}{\partial \xi} + \nabla \cdot (\lambda_o \nabla P_o) = 0, \tag{15}$$

$$\nabla \cdot (\lambda_t \nabla P_o - \lambda_w P_c' \nabla S_w) = 0. \tag{16}$$

To proceed with the LSA, we decompose the perturbed variables S_w and P_o into a base state and a small wavelike perturbation as follows:

$$S_w(\xi, y, t) = \bar{S}(\xi) + \hat{s}(\xi)\cos(2\pi\nu y)e^{\sigma t}, \tag{17}$$

$$P_o(\xi, y, t) = \bar{P}(\xi) + \hat{p}(\xi)\cos(2\pi\nu y)e^{\sigma t}, \tag{18}$$

where $\bar{S}$ and $\bar{P}$ are the solutions of the base-state Equations 12 and 14, respectively, ν is the wavenumber of the perturbation, and σ is its growth rate. We assume the disturbances decay at infinity, i.e. $\hat{s}, \hat{p} \to 0$ for $\xi \to \pm\infty$.

Substituting Equations 17 and 18 into Equations 15 and 16 and linearizing the flow functions (i.e. λ_α and P_c) around $\bar{S}$, we arrive, after considerable algebra, at the eigenvalue problem:

$$\begin{bmatrix} A & B \\ C & D - \sigma \end{bmatrix} \begin{Bmatrix} \hat{p} \\ \hat{s} \end{Bmatrix} = 0, \tag{19}$$

where A, B, C, and D are linear operators of the type $L = L_2\frac{d^2}{d\xi^2} + L_1\frac{d}{d\xi} + L_0$. The coefficients $A_0, A_1, \ldots$ are given by:

$$
\begin{aligned}
A_2 &= \lambda_t, \\
A_1 &= \lambda_t' \frac{\mathrm{d}\bar{S}}{\mathrm{d}\xi}, \\
A_0 &= -4\pi^2\nu^2\lambda_t, \\
B_2 &= -\lambda_w P_c', \\
B_1 &= \lambda_t' \frac{\mathrm{d}\bar{P}}{\mathrm{d}\xi} - 2\left(\lambda_w' P_c' + \lambda_w P_c''\right)\frac{\mathrm{d}\bar{S}}{\mathrm{d}\xi}, \\
B_0 &= \lambda_t' \frac{\mathrm{d}^2\bar{P}}{\mathrm{d}\xi^2} + \lambda_t'' \frac{\mathrm{d}\bar{S}}{\mathrm{d}\xi}\frac{\mathrm{d}\bar{P}}{\mathrm{d}\xi} - \left(\lambda_w'' P_c' + 2\lambda_w' P_c'' + \lambda_w P_c'''\right)\left(\frac{\mathrm{d}\bar{S}}{\mathrm{d}\xi}\right)^2 \\
&\quad - \left(\lambda_w' P_c' + \lambda_w P_c''\right)\frac{\mathrm{d}^2\bar{S}}{\mathrm{d}\xi^2} + 4\pi^2\nu^2\lambda_w P_c', \\
C_2 &= -\lambda_o, \\
C_1 &= -\lambda_o' \frac{\mathrm{d}\bar{S}}{\mathrm{d}\xi}, \\
C_0 &= 4\pi^2\nu^2\lambda_o, \\
D_2 &= 0, \\
D_1 &= v_s - \lambda_o' \frac{\mathrm{d}\bar{P}}{\mathrm{d}\xi}, \\
D_0 &= -\lambda_o'' \frac{\mathrm{d}\bar{S}}{\mathrm{d}\xi}\frac{\mathrm{d}\bar{P}}{\mathrm{d}\xi} - \lambda_o' \frac{\mathrm{d}^2\bar{P}}{\mathrm{d}\xi^2}
\end{aligned}
\tag{20}
$$

We can solve the system in Equation 19 by discretizing the linear operators using a finite difference:

$$
\begin{bmatrix} \boldsymbol{A} & \boldsymbol{B} \\ \boldsymbol{C} & \boldsymbol{D} - \sigma \boldsymbol{I} \end{bmatrix} \begin{Bmatrix} \hat{\boldsymbol{p}} \\ \hat{\boldsymbol{s}} \end{Bmatrix} = \boldsymbol{0}, \tag{21}
$$

where $\boldsymbol{A}$, $\boldsymbol{B}$, $\boldsymbol{C}$, and $\boldsymbol{D}$ are square matrices of size $N \times N$, with N being the number of grid points in the ξ direction, and $\hat{\boldsymbol{p}}$ and $\hat{\boldsymbol{s}}$ are column vectors of size N with the discrete solution of $\hat{p}$ and $\hat{s}$. Assuming that $\boldsymbol{A}$ is invertible, we can solve for $\hat{\boldsymbol{p}}$ to obtain:

$$
\hat{\boldsymbol{p}} = -\boldsymbol{A}^{-1}\boldsymbol{B}\hat{\boldsymbol{s}}. \tag{22}
$$

Substituting Equation 22 into the second row of Equation 21 we arrive at the standard eigenvalue problem:

$$
\boldsymbol{M}\hat{\boldsymbol{s}} = \sigma\hat{\boldsymbol{s}}, \quad \boldsymbol{M} = \boldsymbol{D} - \boldsymbol{C}\boldsymbol{A}^{-1}\boldsymbol{B}. \tag{23}
$$

The dispersion relation is given by the largest positive eigenvalue σ of $\boldsymbol{M}$ for every possible value for wavenumber ν, and for the unbounded domain, that is any real value. For the case where flow is bounded laterally by two impermeable walls at $y = \pm L_y/2$, the no-flux boundary conditions must be satisfied, which translates to:

$$
\left.\frac{\partial S_w}{\partial y}\right|_{y=\pm\frac{L_y}{2}} = \left.\frac{\partial P_o}{\partial y}\right|_{y=\pm\frac{L_y}{2}} = 0. \tag{24}
$$

Satisfying the no-flux boundary conditions limits the possible values for ν to:

$$
\nu = \frac{n}{L_y}, \quad n = 1, 2, 3, \ldots \ . \tag{25}
$$

For numerical simulations of fingers seeded by wavelike perturbations, the perturbation wavenumbers must be restricted to those given by Equation 25 so that the simulation conditions match those of the LSA.

S2 Growth rate and finger size calculation

To calculate the growth rate of the fingers, we turn to the vorticity field, $\boldsymbol{\omega}=\nabla\times\boldsymbol{u}_t$, which for the two-dimensional homogeneous case (no gravity) can be written as:

$$\boldsymbol{\omega} = \frac{1}{\lambda_t}\frac{\mathrm{d}\lambda_t}{\mathrm{d}S_w}\nabla S_w \times \boldsymbol{u}_t = -\frac{\mathrm{d}\lambda_t}{\mathrm{d}S_w}\nabla S_w \times \nabla P_o. \tag{26}$$

Substituting the perturbed variables S_w and P_o (Equations 17 and 18) into Equation 26 and linearizing the flow functions around the base state, we can write the vorticity field as:

$$\boldsymbol{\omega} = 2\pi\nu\frac{\mathrm{d}\lambda_t}{\mathrm{d}S_w}\left(\frac{\mathrm{d}\bar{S}}{\mathrm{d}\xi}\hat{p} - \frac{\mathrm{d}\bar{P}}{\mathrm{d}\xi}\hat{s}\right)\sin(2\pi\nu y)e^{\sigma t}\hat{\boldsymbol{z}} = \hat{\omega}(\xi,y)e^{\sigma t}\hat{\boldsymbol{z}}, \tag{27}$$

where $\hat{\boldsymbol{z}}$ is the unit vector in the z direction normal to the plane of flow. We can see that the vorticity field has the same growth rate as the fingers at the onset of the instability.

With the norm of the vorticity field defined as [2]:

$$\|\boldsymbol{\omega}\|(t) = \left(\int_{-\frac{L_y}{2}}^{\frac{L_y}{2}}\int_{-\infty}^{\infty}\left(\hat{\omega}(\xi,y)e^{\sigma t}\right)^2 d\xi dy\right)^{\frac{1}{2}} = e^{\sigma t}\|\hat{\omega}(\xi,y)\|, \tag{28}$$

the growth rate of the fingers can then be calculated by:

$$\sigma = \frac{\mathrm{d}}{\mathrm{d}t}\ln\|\boldsymbol{\omega}\|, \tag{29}$$

Although our simulations are formulated in the fixed frame (x,y) rather than the moving frame (ξ,y), $\hat{\omega}$ is nonzero only in the vicinity of the shock front—where the eigenfunctions $\hat{p}$ and $\hat{s}$ are nonzero—so $\|\boldsymbol{\omega}\|$ can be computed as:

$$\|\boldsymbol{\omega}\| = \sqrt{\sum_{i=1}^{N_x}\sum_{j=1}^{N_y}\omega_z(x_i,y_j,t)^2}, \tag{30}$$

where w_z is the z-component of the vorticity field given by Equation 26, and the growth rate of the perturbations can be computed as:

$$\sigma \approx \frac{1}{\Delta t}\ln\left(\frac{\|\boldsymbol{\omega}\|(t)}{\|\boldsymbol{\omega}\|(t-\Delta t)}\right), \tag{31}$$

As shown by Riaz and Tchelepi [3], the dominant mode (or wavenumber), $\hat{\nu}$, of the fingers can be estimated by:

$$\hat{\nu} = \frac{\int_c^\nu \nu E(\nu,t)d\nu}{\int_c^\nu E(\nu,t)d\nu} \tag{32}$$

where $E(\nu,t)$ is the energy spectrum of the disturbed flow, calculated via the Fourier transform of the longitudinally averaged vorticity field given by:

$$E(\nu,t) = \left[\int_{-\frac{L_y}{2}}^{\frac{L_y}{2}}\left(\int_0^{L_x}\omega_z(x,y,t)dx\right)e^{-\mathrm{i}2\pi\nu y}dy\right]^2 \tag{33}$$

Another useful variable for tracking the evolution of the fingers is the *finger size*[1], which we define as the distance between the front of the fingers and the front of the unperturbed case (i.e., the solution to the one-dimensional, Buckley-Leverett equation), as shown in Figure 1.

[1] An obvious way to calculate the growth rate of the fingers is to simply apply Equation 31 to finger size, instead of the vorticity norm. In practice, though, at the early stages, finger size evolution is not an accurate measure, even for very fine grids, because the fingers are still very small. So using the vorticity norm is preferred.

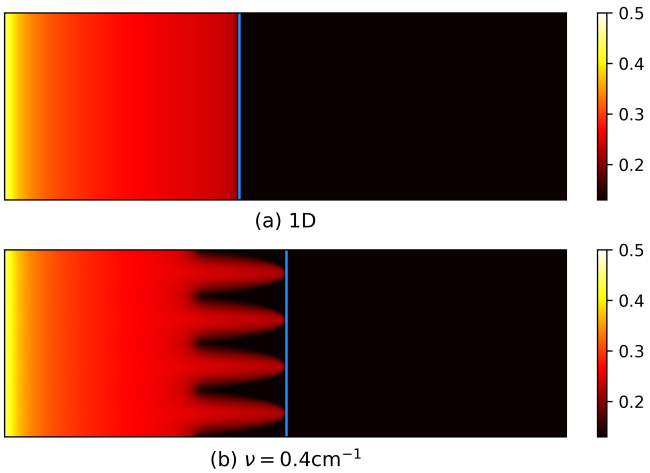

Fig. 1 Saturation maps for the (unperturbed) one-dimensional case and the case with wavelike perturbations ($\nu = 0.4$ cm^{-1}). The blue lines indicate the front most position of the displacements. The distance between the two fronts, at any given instant, gives the finger size.

S3 Nonlinear evolution of immiscible fingers

In this section, we analyse the nonlinear evolution of immiscible fingers generated by wavelike perturbations in a homogeneous porous medium. The model has dimensions $L_x = 30\,\text{cm}$ and $L_y = 10\,\text{cm}$, with cell dimensions of $l_x = l_y = 0.02\,\text{cm}$. For the five rows of cells nearest the inlet (at $x = 0$), the saturation is set to $S_w{=}S_{wf}{-}0.005\cos(2\pi\nu y)$, where S_{wf} is the water saturation at the shock front and ν is the wavenumber of the perturbation ($\nu = n/L_y$, $n = 1, 2, \ldots$). For the remaining cells, the initial saturation is set to $S_w = S_{wr}$ (the residual water saturation). The RP and capillary pressure functions used in this simulation are RP1 and Pc1, respectively.

Figure 2a compares the growth rate of the fingers in the numerical simulations with the growth rate given by the LSA The dashed line plots the dispersion relation given by the LSA, and the dotted line is the dispersion relation when we account for the extra dissipative effects of numerical dispersion on the base-state solution (Equation 12), which is done by adding a numerical diffusion term to the dispersive coefficient D_c (Equation 13) to obtain:

$$D_c^{num} = D_c + D_{num} = \frac{\lambda_w \lambda_o}{\lambda_t} \frac{\mathrm{d}P_c}{\mathrm{d}S_w} - \frac{1}{2} \frac{\mathrm{d}F_w}{\mathrm{d}S_w} \left(\Delta x + \frac{\mathrm{d}F_w}{\mathrm{d}S_w} \Delta t \right), \tag{34}$$

where Δx is the cell size and Δt is the maximum time step used in the numerical simulations (in non-dimensional units). Equation 34 assumes the backward difference, implicit in time scheme [4].

We see that the corrected dispersion relation[2][3] (dotted line) matches the early-time ($t^* = 0.085$) results of the numerical simulations. As the simulation progresses, nonlinear effects become more important and the growth rate of the fingers decreases, eventually reaching zero—i.e., the fingers reach a steady state.

Figure 2b shows how the fingers grow in length over time for each initial wavenumber. At the onset, when the perturbations are small and their growth rates can be well described by the LSA, the size of the fingers is proportional to the growth rate of the initial perturbation. As the simulation progresses, nonlinear effects become more important and the fingers generated from smaller wavenumbers (i.e., larger wavelengths) keep growing, while those generated from larger wavenumbers stagnate at sizes inversely proportional to their wavenumbers.

This is consistent with the weakly nonlinear analysis by Chikhliwala and Yortsos [5], which found that perturbations near the critical wavenumber (ν_{cut}, from linear stability) are supercritical, stabilizing to an equilibrium amplitude (proportional to the mobility ratio at the displacement front). In our simulations, we find that this supercritical stability is not only true in the vicinity of ν_{cut}, but, possibly, for all wavenumbers. Later in this section, we discuss finger stagnation in more detail.

In Figure 2, we see that the growth rates and finger size curves display erratic behaviour for the low and high wavenumbers cases. This is driven by finger splitting, in the case of low wavenumbers, and by finger merging in the case of high wavenumbers. To better visualize these effects, as well the behaviour of the intermediate wavenumbers, we show, in Figure 3, the vorticity maps for the cases with ν=0.1, 0.3, 0.6 and 1.2 cm^{-1}, at different times during the simulation.

[2] Note that only the base-state solution is corrected, while the coefficients of the linear operators in the eigenvalue problem (Equation 20) remain unchanged.

[3] Although we do not show it here, we observe that the impact of numerical dispersion diminishes in the non-linear regime, and so its impact on finger evolution is less significant.

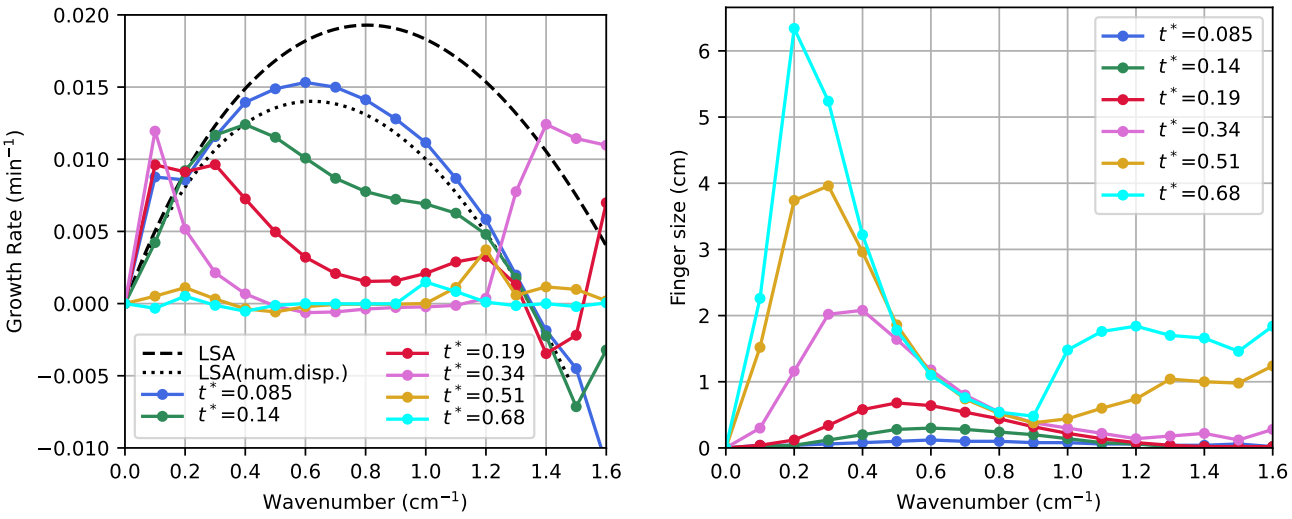

(a) Growth rate

(b) Finger size

Fig. 2 Growth rate and size of the fingers at different times, for different wavenumbers, for the homogeneous model. The time for breakthrough (t_{bt}) is 1770 min and corresponds to 0.156 PVI.

If we compare the fingers of the ν=0.3 cm^{-1} and ν=0.6 cm^{-1} cases, we see that the thicker fingers (ν=0.3 cm^{-1}), which initially grow slower than those from ν=0.6 cm^{-1}, maintain their growth and eventually become larger than those from ν=0.6 cm^{-1}, which stagnate in size after t^*=0.3.

For the case with ν=1.2 cm^{-1}, the fingers stagnate at much smaller values than those seen in the case with ν=0.6 cm^{-1}. That means the accumulation of numerical errors during the simulation is enough to distort the displacement front, causing some fingers to grow larger than their neighbours (t^*=0.4), which leads to shielding effects, where the larger fingers impede the growth of their smaller neighbours. As the simulation progresses, the smaller fingers eventually merge into the larger ones. This behaviour is consistent with the findings of Riaz and Tchelepi [3] and can be seen in Figure 4, which tracks the evolution of the dominant modes ($\hat{\nu}$) for cases with different initial perturbations. We see that for the ν=1.2 cm^{-1} case, the dominant mode suddenly decreases at around t^*=0.4, indicating the merging of the fingers. The same is seen for the ν=0.9 cm^{-1} case, at around t^*=0.8. As can be seen in Figures 2 and 4, this collapse in $\hat{\nu}$ does not happen for cases with initial perturbations with $\nu \leq 0.8\,\mathrm{cm}^{-1}$, because the fingers generated from these perturbations are large enough to be unaffected by numerical errors (at least before breakthrough time).

The case with ν=0.1 cm^{-1}, which should display only one finger in the simulation, displays, instead, six fingers—which corresponds to the fastest growing wavenumber at the onset of instability, ν=0.6 cm^{-1}. This is a clear example of tip splitting where small numerical errors seed new fingers that grow faster than the original one, and explains the erratic behaviour of the growth rate for low wavenumbers in Figure 2a. Because the fingers generated are not of equal size, the larger ones eventually "shield" the smaller ones, which leads to a decrease in the dominant wavenumber of the fingers as the simulation progresses. This can be observed in Figure 4, where we see that the calculated $\hat{\nu}$ of the ν=0.1 cm^{-1} case starts to decline after it reaches a maximum of $\hat{\nu} \approx 0.6\,\mathrm{cm}^{-1}$, at around t^*=0.5.

In Figure 5, we plot the maximum size of the fingers (before numerical instability provokes merging) as a function of the initial wavenumber, and we can see a power-law relation between the maximum size and the wavenumber (with an exponent of approximately 2.5), showing that the thicker (low wavenumber) fingers can grow substantially larger than the thinner (large wavenumber) ones. That fingers growth ceases in the nonlinear regime agrees with the weakly nonlinear analysis in Chikhliwala and Yortsos [5]. Although their analysis was limited to wavenumbers near the cut-off wavenumber, they find that perturbations with an unstable wavenumber eventually reach an equilibrium amplitude (A_{eq}) in the nonlinear regime, even if the initial perturbation amplitude was larger than A_{eq}. Our simulations show that this seems to be true for all unstable wavenumbers (though our grid dimensions limit the minimum wavenumbers we can check). The physical mechanism that arrests growth is relatively straightforward. As is known from LSA, transverse diffusion scales with the square of the wavenumber, which is what eventually leads to a cut-off wavenumber (ν_{cut}) that does not destabilize the displacement. Although at the onset of the instability, such diffusive flow is not enough to arrest finger growth for cases where $\nu < \nu_{cut}$, as the fingers elongate (keeping their width) and the displacement front deforms, the total area (or perimeter) of the front increases, increasing the total transverse diffusive flow, at some point stabilizing the fingers. Although the fact that our power-law fit gives an exponent of 2.5, not 2, suggests some other nonlinear/geometrical effects are in play.

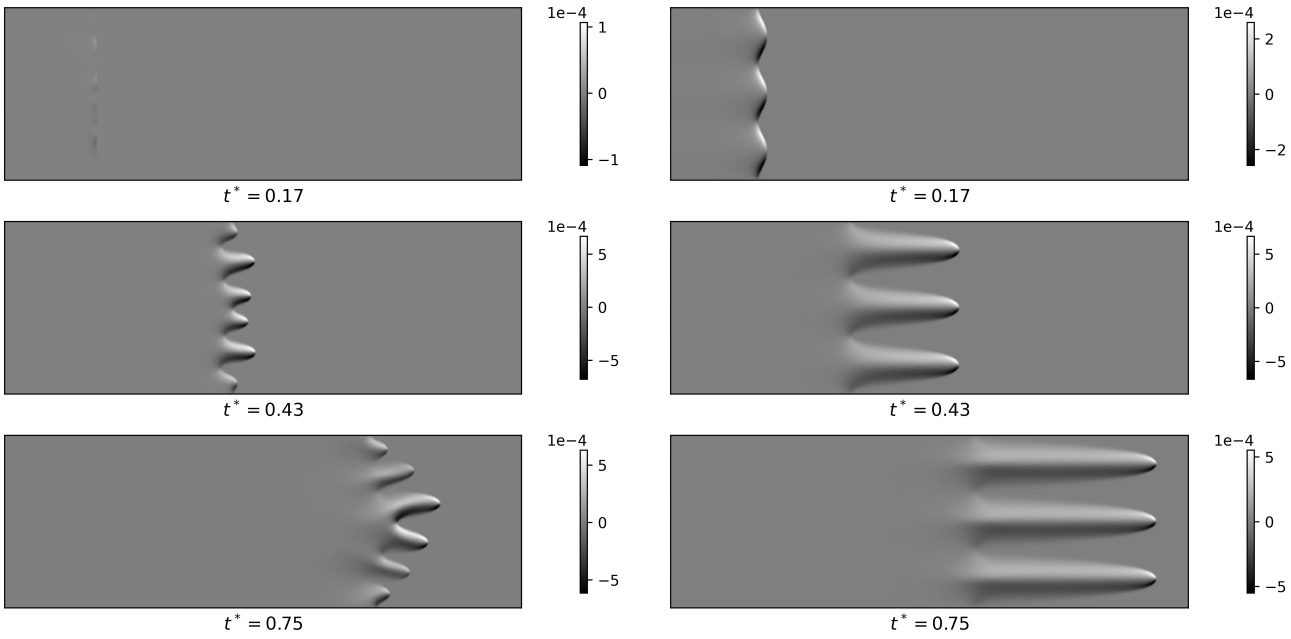

(a) ν=0.1 cm^{-1} (b) ν=0.3 cm^{-1}

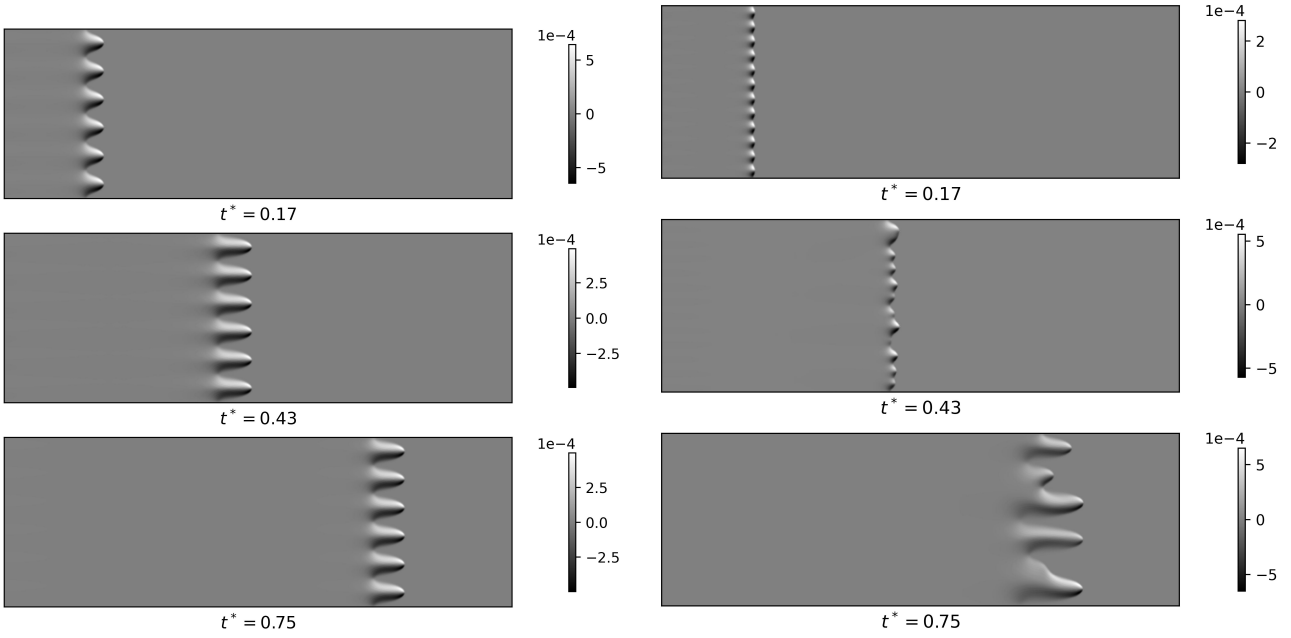

(c) ν=0.6 cm^{-1} (d) ν=1.2 cm^{-1}

Fig. 3 Vorticity maps for the cases with ν=0.1, 0.3, 0.6 and 1.2 cm^{-1}, at different times during the simulation.

The arrest of finger growth in the nonlinear regime is conditional on the fingers maintaining their uniformity during the simulation, although the fact that transverse diffusion (the main stabilizing mechanism) is increased by the elongation of the fingers is not limited to the uniform fingers' scenario. In fact, as can be seen in [3], when fingers are randomly seeded, the longer fingers not only suppress the growth of their smaller neighbours by shielding effects, but also grow in thickness as they grow in length, eventually absorbing the smaller fingers. In summary, the widening of the fingers (causing merging) is linked with their ability to grow longer.

Another interesting observation about the calculated $\hat{\nu}$ for the ν=0.3, 0.6 and 0.9 cm^{-1} cases (Figure 4), is the gradual increase in $\hat{\nu}$, with an eventual stabilization at a new, higher value than the original perturbation wavenumber. This is because, as the fingers grow, their shapes start to deviate from the original cosine shape. This increases the value for $\hat{\nu}$ calculated from Equation 32, even if the number of fingers remain unchanged.

We exemplify this in Figure 6, which shows, for the case with ν=0.3 cm^{-1}, at $t^* = 0.1$ and $t^* = 0.51$: the saturation distribution; the isoline S_w=0.18 (midway between $S_{w0} = 0.13$ and $S_{ws} = 0.24$) that defines the profile

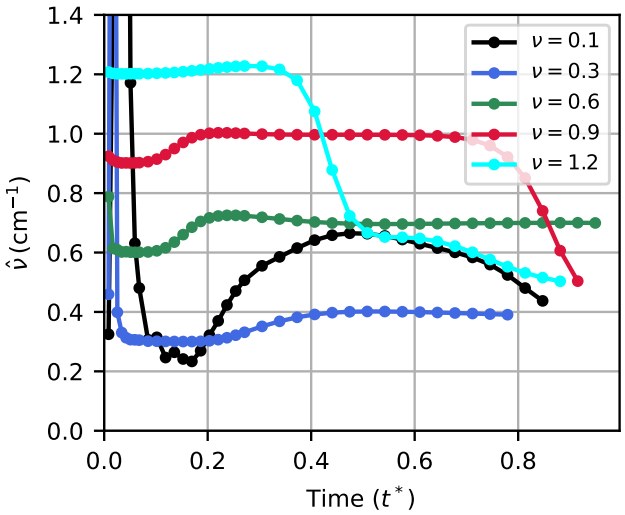

Fig. 4 Evolution of the dominant wavenumber of the fingers over time. Each curve is shown up to the corresponding breakthrough time.

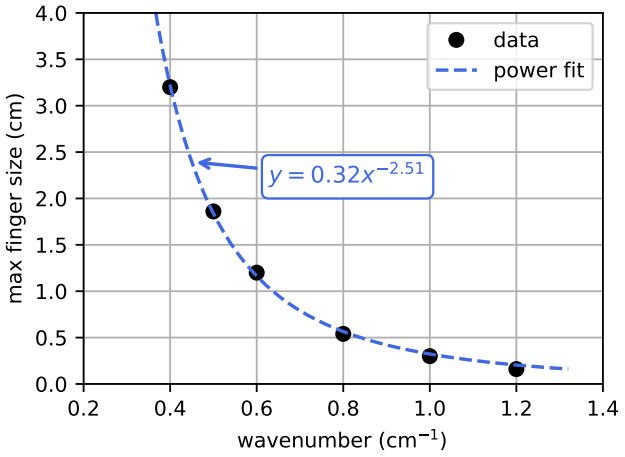

Fig. 5 Maximum finger size as a function of initial wavenumber. Simulation results and the fitted power-law relation.

of the fingers/displacement front; the Fast Fourier Transform (FFT) of the isoline; and the curvature κ, given by:

$$\kappa = \frac{\mathrm{d}^2 x}{\mathrm{d}y^2} \frac{1}{\left(1 + (\mathrm{d}x/\mathrm{d}y)^2\right)^{3/2}}. \tag{35}$$

We see that as the fingers grow, the profile of the fingers (the isoline) deviates from a cosine-type curve, which leads to higher modes appearing in the Fourier transform of this profile, increasing the average value of the dominant mode, and accounts for the observed behaviour in Figure 4. The fingers also become "sharper" as they grow longer (but retain their width), which is reflected in the increasing curvature. The tips of the fingers become more rounded as they grow, which can be seen more clearly in Figure 7, where we plot the normalized dimensions and curvature (not normalized) of one finger of the ν=0.4 cm^{-1} case, for three different times.

To understand the impact of a curvature at the front, we change to a coordinate system that follows the curved front of the fingers,

$$\boldsymbol{r}(s, \eta, t) = \boldsymbol{r}_f(s, t) + \eta \hat{\boldsymbol{n}}(s, t), \tag{36}$$

where $\boldsymbol{r}_f(s,t)$ is the position of an isoline S_w=S_{wf} at the displacement front, s is the curvilinear coordinate along the isoline, $\hat{\boldsymbol{n}}(s,t)$ is the unit vector normal (pointing outwards) to the isoline at s, and η is the signed normal distance. The Frenet-Serret relations gives us:

$$\frac{\mathrm{d}\hat{\boldsymbol{t}}}{\mathrm{d}s} = -\kappa \hat{\boldsymbol{n}}, \quad \frac{\mathrm{d}\hat{\boldsymbol{n}}}{\mathrm{d}s} = \kappa \hat{\boldsymbol{t}}, \tag{37}$$

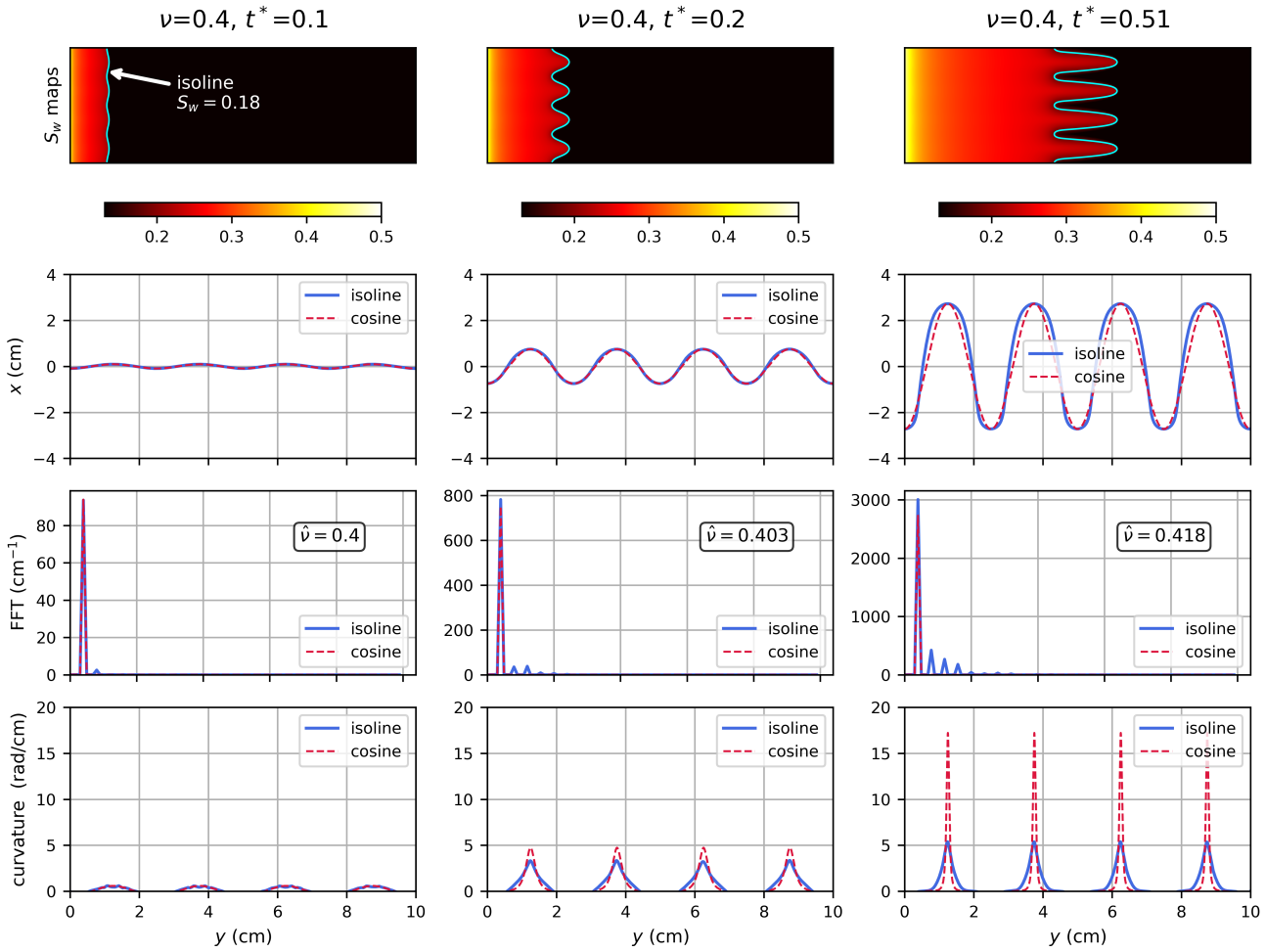

Fig. 6 Saturation, finger profile and curvature for the ν=0.4 cm^{-1} case, at two different times during the simulation. For each time, the top graph shows the S_w maps and an isoline at S_w=0.18 (shown in blue). The second (from the top) graph compares the isoline shape with the cosine function. The third graphs compare the FFT of the isoline and cosine function. And the last graph shows the positive values of the curvature along the isoline.

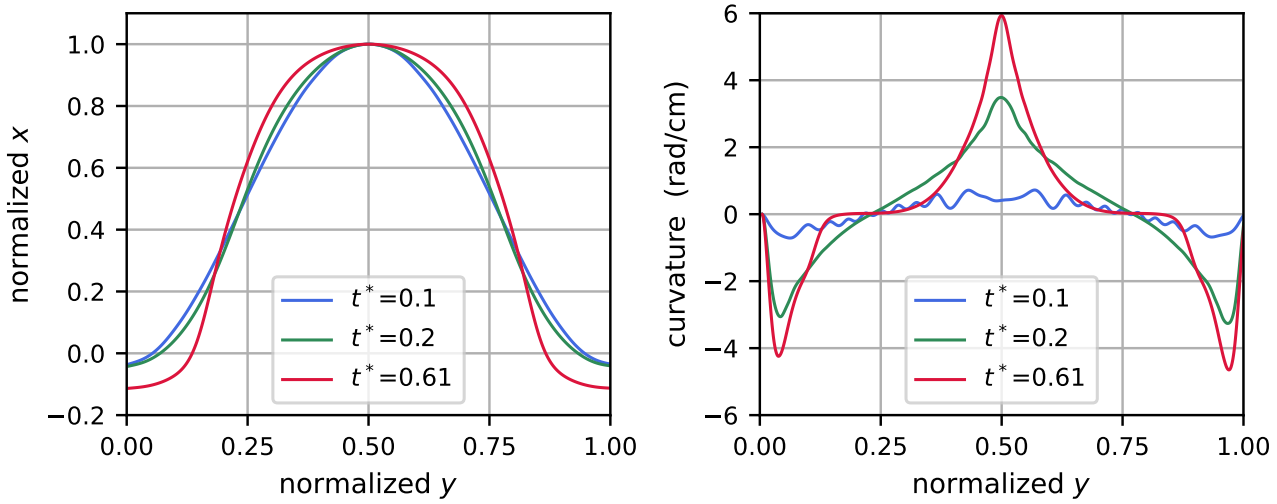

Fig. 7 Normalized dimensions and curvature of one finger of the ν=0.4 cm^{-1} case, for three different times during the simulation.

where $\hat{\boldsymbol{t}}(s,t)=\mathrm{d}\boldsymbol{r}_f/\mathrm{d}s$ is the unit vector tangent to the isoline, $\kappa=\kappa(s,t)$ is the curvature of the isoline. Assuming that the transition zone at the front is small compared to the radius of curvature, i.e. $\eta/R = \eta\kappa \ll 1$, and that $\partial_s S_w$ and $\partial_{ss} S_w$ are small near η=0, we can write the diffusive term in the advection-diffusion equation as:

$$\nabla \cdot (D_c \nabla S_w) \approx \frac{\partial}{\partial \eta}\left(D_c \frac{\partial S_w}{\partial \eta}\right) + \kappa D_c \frac{\partial S_w}{\partial \eta}, \tag{38}$$

where D_c is the dispersive coefficient given by Equation 13.

The $\kappa D_c \partial(S_w/\partial\eta)$ of the above equation gives us the impact of the curvature. Given that $D_c < 0$, at the tip of the fingers, where $\kappa > 0$, this term acts as a convective term on the *opposite* direction of flow. Conversely, at the region between the fingers, where $\kappa < 0$, the curvature adds a convective term in the *same* direction of flow. In both cases, the curvature has a stabilizing effect. This helps explain why the tip of the fingers become more rounded as they grow, as seen in Figure 6. As can be seen by the comparison between the isoline and the cosine function curvatures (bottom-right graph), the curvature at the tip of the cosine function is much greater than at the tip of the isoline. This peak of curvature at the tip would mean a concentrated stabilizing flow at the tip, eventually "rounding" the shape of the fingers.

Interestingly, Figure 8 shows that though the dimensions of the stagnated fingers differ considerably for the cases with ν=0.4, 0.6 and 0.8 cm^{-1}, their curvatures at their tips are similar, which suggests a local balance is reached at the tips of the fingers, and that this balance is independent, or weakly dependent, of the wavelength (or finger thickness). Further support for this hypothesis of local balance comes from analysing the curvature of fingers seeded from random perturbations, shown in Figure 9. We can observe that, though the fingers keep growing and merging, the maximum curvature values at the tip remain relatively constant after some time, and very similar to the maximum curvature values observed for the wavelike perturbations.

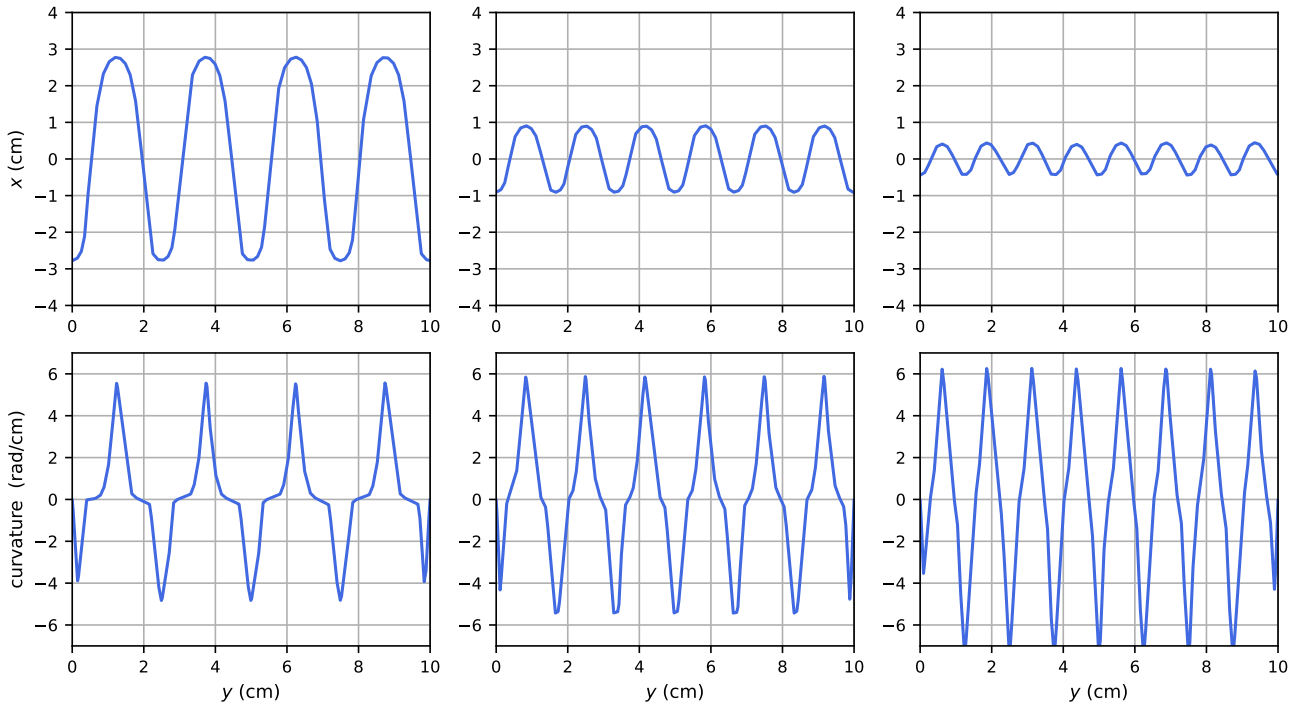

Fig. 8 Finger profile and curvature for the cases with ν=0.4, 0.6 and 0.8 cm^{-1}, after finger growth has ceased.

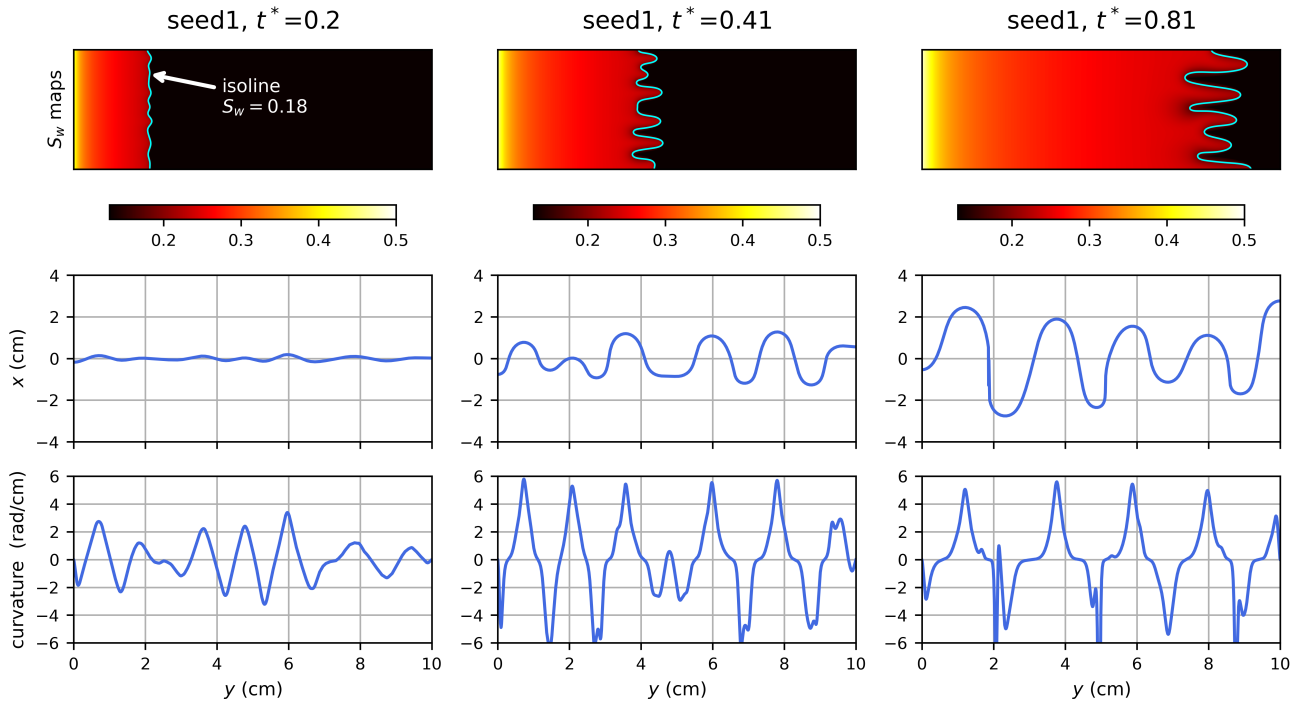

Fig. 9 Saturation, finger profile and curvature for the case with random perturbations at the inlet. For each time, the top graph shows the S_w maps and an isoline at S_w=0.18 (shown in blue). The second (from the top) graph compares the isoline shape with the cosine function. And the last graph shows the curvature along the isoline.

References

[1] Riaz, A., Tchelepi, H.A.: Linear stability analysis of immiscible two-phase flow in porous media with capillary dispersion and density variation. Physics of Fluids **16**(12), 4727–4737 (2004) https://doi.org/10.1063/1.1812511

[2] Riaz, A., Meiburg, E.: Radial source flows in porous media: Linear stability analysis of axial and helical perturbations in miscible displacements. Physics of Fluids - PHYS FLUIDS **15** (2003) https://doi.org/10.1063/1.1556292

[3] Riaz, A., Tchelepi, H.A.: Numerical simulation of immiscible two-phase flow in porous media. Physics of Fluids **18**, 014104 (2006) https://doi.org/10.1063/1.2166388

[4] Lantz, R.B.: Quantitative evaluation of numerical diffusion (truncation error). Society of Petroleum Engineers Journal **11**(3), 315–320 (1971) https://doi.org/10.2118/2811-PA

[5] Chikhliwala, E.D., Yortsos, Y.C.: Investigations on viscous fingering by linear and weakly nonlinear stability analysis. SPE Reservoir Engineering **3**(4), 1268–1278 (1988) https://doi.org/10.2118/14367-PA